

Chapter 2

Unsupervised Retinal Blood Vessel Segmentation

2.1 Introduction

Diagnosis of any disease requires a complete understanding of the basic anatomy of the affected organ. In the case of diseases like DR, Glaucoma, AMD, and RoP, the retina of the eye gets affected. Thus, understanding of the retinal layer plays a crucial role. The retina is a thin layer of tissues present as the inner lining at the back of the eye. Typical features of retina includes, blood vessels, Optic disc (OD), macula, fovea, etc. The progression of the disease may develop abnormal features in the retinal layer. This can be studied using a 2-D projection of the retinal layer called fundus image. The term fundus is used for the back portion of any hollow organ. In the case of the eye, fundus means the retinal layer (or retina).

Fundus image provides a non-mydriatic way to study the retina. The occurrence of abnormalities can be observed using various image analysis techniques on a fundus image. Vessel segmentation is one of the preliminary steps in retinal disease diagnosis. It is important because extracted vessel map may show some abnormal structural changes, or if it is normal, then it can be removed from the retinal image to focus more on other abnormal features. Thus, vessel segmentation is a vital step in the diagnosis of any retinal disease.

An RGB fundus image appears red-orange because of the orange choroidal layer present in the background. OD is a bright yellowish, disc-shaped structure present in the retina. Through OD, millions of nerve fibers pass from the eye to the brain, and major blood vessels enter to nourish the retinal layer simultaneously. On moving further, retinal blood vessels enter through the OD divide and spread in a dichotomous pattern (Y-shaped). Blood vessels are fine tubular structures, circulating blood throughout our body and so in the retina. Retinal vessels are structurally complicated, as they can be seen as branches of a tree with continuously varying width, thickest at their origin and thinnest at the ends. Thin vessels are poorly contrasted in fundus images; they almost blend in the retinal background. These factors make the segmentation of blood vessels very difficult, even in the case of a healthy eye. An unhealthy retina develops abnormalities like micro-aneurysms, soft and hard exudates (bright lesions), drusens, hemorrhages (dark lesions), venous beading, abnormal vessel growth, etc. In the presence of these pathological features, blood vessel segmentation becomes much more challenging.

Researchers have explored a wide spectrum of segmentation techniques for extracting vessel-like structures. Moccia et al. [2] have presented a noteworthy review on the same. These techniques can be broadly classified into unsupervised and supervised methods. Under the category of unsupervised methods, there are methods based on matched filtering (MF), morphology, profile-modeling, active contour, multi-scale, etc. In MF-based methods, vessel's cross-sectional intensity profile is matched with a suitable filter. Chaudhuri et al. [6] assumed vessels to be piece-wise linear and have Gaussian intensity profile, Hoover et al. [8] proposed iterative threshold probing on the MF response image, Zhang et al. [9] gave MF-FDOG (Matched Filter-First order Derivative Of Gaussian) based method in which matched filter response is thresholded using the first-order derivative of Gaussian response. Chakraborti et al. [59] proposed a self-adaptive matched filter for vessel segmentation. Most of the MF methods assume a Gaussian vessel profile, which may not be the best match in many cases. This mis-match leads into loss true positives. Also, the regions like edges of OD, which have vessel-like profiles, may lead into generation of false positives. Morphological

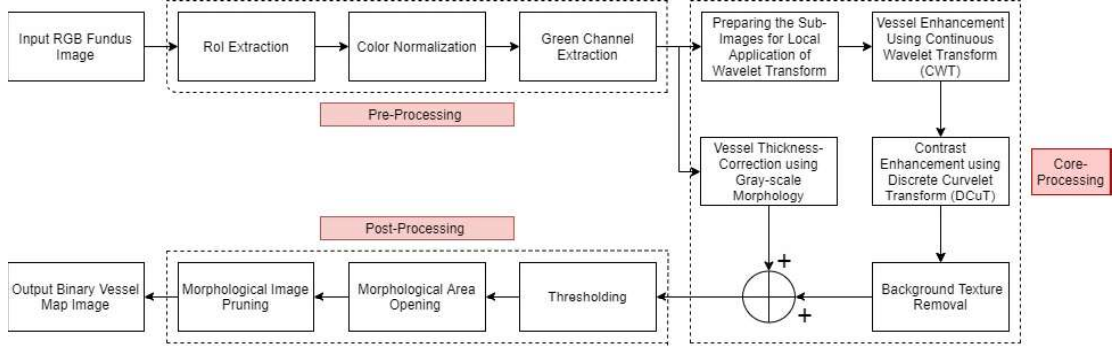


Figure 2.1: *Block diagram of the proposed unsupervised vessel segmentation algorithm. The diagram shows three major blocks: pre-processing (RoI extraction, color normalization, green channel extraction), core-processing (CWT, DCuT, morphological thickness correction), and post-processing (thresholding, morphological opening, pruning)*

methods are comparatively fast. They generally assumed the vessel structure as linear. However, they do not exploit the vessel's cross-sectional profile, which led into their limited performance. Zana et al. [18] used mathematical morphology along with cross curvature evaluation to segment vessel-like structures. Mendonca et al. [22] exploited the concept of morphological reconstruction to extract the retinal vessel map. Another set of methods based on vessel profile modeling and tracing are observed to provide a good estimation of vessel width. However, such methods require seed points to begin tracing and also end point, which is mostly done manually. Delibasis et al. [29] presented a ‘stripe’ based parametric vessel model to trace and estimate vessel along with its diameter. Other conventional image processing based methods like [30], [31], [12], [61], [60], [48], etc. have performed well but are observed to be computationally expensive.

In supervised vessel extraction techniques, researchers have explored various conventional machine learning algorithms [23], [13], [10], [24], [32], etc. Soares et al. [23] evaluated 2-D Gabor wavelet transform coefficients at multiple scales, and then Gaussian Mixture Model (GMM) based classifier is applied for pixel-wise classification. Fraz et al. [13] gave an ensemble system of decision trees. Here, the feature vector is based on the orientation analysis of gradient vector field, morphological transformation, line strength measures, and Gabor filter responses. Staal et al. [10] extracted image ridges and then applied k-Nearest Neighbour (k-NN) algorithm to classify the feature vectors.

Ricci et al. [24] employed a fixed-length line detector at different orientations and then used a support vector machine (SVM) classifier for pixel-wise classification. Marin et al. [32] designed a neural network classifier using gray-level and moment invariants-based 7-D feature vector, representing each pixel. Kar et al. [17] has used curvelet transforms for blood vessel extraction. These methods have revolutionized the vessel extraction by improving the segmentation performance by a large extent specially in terms of area under the Receiver Operating Characteristic curve parameter. However, the feature engineering demands manual intervention by doing appropriate feature extraction along-with weight adjustments with change in training images. In recent years, the supervised methods have evolved from conventional machine learning techniques to automated deep learning methods. In deep learning, the machine itself does the end-to-end job of pattern recognition by automatic feature extraction [33], [50], [39], [34], [40], etc. Here, the manual intervention is eliminated, and the model can extract very low level features, which otherwise were impossible to address. However, unfortunately, these methods are controlled by the amount of labeled data available and in medical domain, there is scarcity of pixel level annotated data.

Vessel segmentation is still an active area of research because of subjective nature of the problem. There is still a need for a generic as well as precise vessel extraction algorithm, which is independent of the subject. Supervised methods have performed very well, but most of them face data-limitations. Unsupervised methods do not need any data, but they fail in generalising their results. Also, in-spite of many unsupervised methods in literature, none of them have specifically focused on the ‘completeness’ of the vessel map. In other word, the thin vessel endings which are crucial from the aspect of the DR diagnosis, have not been focused on, as loss of these vessels do not affect the accuracy parameter. In this chapter, we propose a robust vessel segmentation algorithm focusing on extracting the complete retinal vessel map, which includes prominent vessels along with the low-contrast, fine vessel-endings. Here, we exploit two multi-scale transforms (wavelets and curvelets) for segmenting the vessels in a novel manner. Real coefficients of 2-D Gabor wavelet transform are evaluated and processed at sub-image level (locally), which improves the extraction of poor-contrast,

thin vessel-endings. Further, the curvelet transform of the integrated wavelet-enhanced image (global application) is used to suppress the coarse, non-vessel background, which enhances the contrast of the gray-scale vessel map. The resulting vessel response is combined with a morphological response to recover the major vessel widths. The separate handling of thin and thick vessels makes this algorithm unique and more promising. In addition, this work proposes an adequate combination of preprocessing steps (generic FoV and RoI extraction, color normalization, etc.) to make the algorithm more robust. The proposed vessel segmentation method is tested and evaluated on four public datasets, DRIVE [11], STARE [8], CHASE-DB1 [13] and HRF [48], and it has proved its robustness by maintaining a high value of average accuracy, sensitivity, specificity, precision, F-1 score, G-mean, MCC and AUC-ROC on all sets of data. In terms of these metrics, this method has outperformed many state-of-the-art retinal blood vessel segmentation techniques, which includes some break-through supervised methods too. Being unsupervised makes this algorithm subject-independent, which places it in an advantageous position over all other supervised and deep learning state-of-the-art methods.

2.2 Proposed Method for Unsupervised Vessel Extraction

Blood vessels are examples of curve singularities. They are tubular structures of continuously varying width (mostly decreasing). Segmentation of a complete vessel map using 2-D images is a challenging task. During extraction of major vessel arcade (thick vessels), it is difficult to extract the complete thickness, i.e., till the boundary pixels. Extraction of thin vessels is even more challenging because of the poor contrast between vessel foreground and non-vessel background. Also, sometimes, arbitrary orientation or high tortuosity of vessels can amplify the problem. The presence of pathology may worsen the situation.

In this work, we have proposed a generic algorithm (tested on diverse sets of fundus images) that segments both thin and thick retinal blood vessels efficiently. The signifi-

cance of this work lies in the fact that we have developed a feature-based, unsupervised algorithm using conventional image processing techniques. This makes the proposed work subject-independent, which fulfills a crucial need for automatic medical image segmentation. It does not require any kind of supervision of labeled data.

The presented algorithm, broadly, works in three stages: pre, core, and post-processing. Figure 2.1 describes the steps involved in the proposed algorithm in the form of a block diagram. The following sections discuss this work in detail.

2.2.1 Pre-processing

Pre-processing involves some initial refining steps to convert the raw input into the process-able form. Generally, these steps are application-specific. In our case, other than camera artifacts, captured fundus images may have certain issues which affect the vessel segmentation process. Some of these are non-uniform color, too bright/too dull illumination, poor contrast, or some form of noise. Various techniques of image processing can be used to handle them. Such pre-processing of data before applying the core algorithm helps in improving the performance of the algorithm. In our case, input data is in the form of a color image. We assume $\{I(x, y) | x, y \in \mathbb{Z}\}$ to be the raw digital input RGB fundus image. Pixel intensity values in all the channels are normalized and lie in the range of $[0, 1]$. The following sub-sections discuss the three steps of pre-processing applied to our data.

RoI Extraction

The very first step of pre-processing is to discard the non-informative, redundant pixels outside the FoV in the fundus image. This helps in dealing with the time complexity and allows us to work only on the required pixels. The area inside the FoV is our RoI which contains all the information. To extract the RoI and suppress all the outer pixels, we need a binary mask image. Here, we have proposed a generic FoV mask using the color information of the fundus image. A pixel-wise weighted combination of

all the three channels of RGB color space is obtained, as described in eq. (1).

$$I_m(x, y) = w_1 I_r(x, y) + w_2 I_g(x, y) + w_3 I_b(x, y), \forall(x, y) \quad (2.1)$$

where, $I_m(x, y)$ denotes the weighted combination of all the three channel intensities, $I_r(x, y)$, $I_g(x, y)$ and $I_b(x, y)$ are the intensity images of red, green and blue channel, respectively and w_1 , w_2 and w_3 are their corresponding weights. These weights are optimized by minimizing the mean square error, using publicly available ground truth of FoV masks. This combination image $I_m(x, y)$ eases the generation of binary mask image $mask(x, y)$ by using a single-valued intensity threshold t_I . This threshold value is calculated using Otsu method [47],

$$mask(x, y) = \begin{cases} 1, & I_m(x, y) > t_I \\ 0, & \text{Otherwise} \end{cases}, \forall(x, y) \quad (2.2)$$

This binary mask is used to extract the ROI for vessel segmentation. Also, the diameter of the obtained binary mask helps us in deciding some parameters for the algorithm. Figure 2.2 shows obtained binary masks corresponding to example RGB fundus images taken from different datasets. Figure 2.2 (a) shows the ‘01_test’ image from the DRIVE dataset and its corresponding binary mask image. Similarly, Figure 2.2 (b), (c), and (d) illustrate the binary mask images corresponding to image ‘im0077’ from STARE, ‘Image_05L’ from CHASE_DB-1, and image ‘08_dr’ from the HRF dataset, respectively.

Color Normalization

After ROI extraction, another important pre-processing step is to normalize color information of fundus images belonging to different databases. In the real world, images are captured differently. The difference in imaging conditions like camera used, light illumination of the nearby area, geographical location of the experiment, age group of the subject are some factors that make images of each dataset different. Though the basic anatomy of the eye remains the same, color values, dimensions, and intensity illumination may vary. Thus, this step of normalization is important to generalize our

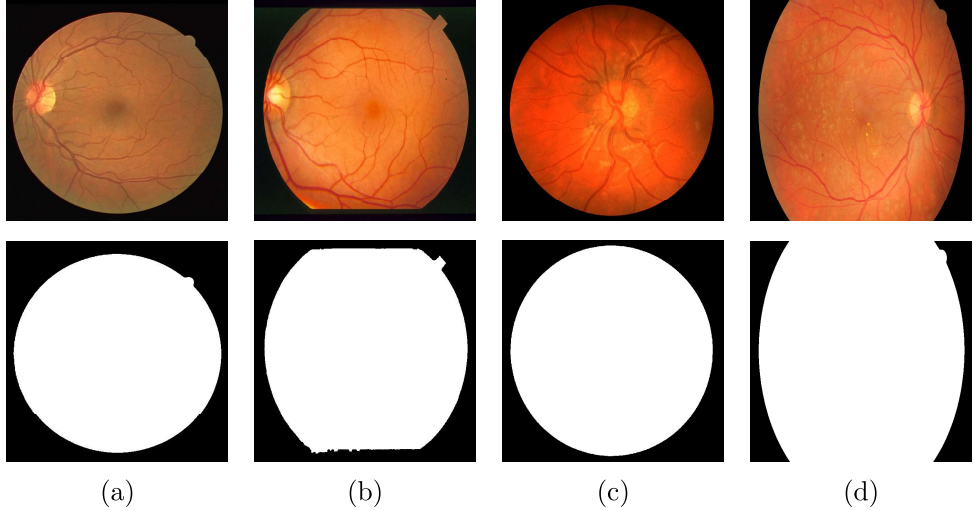


Figure 2.2: *Illustration of derived binary masks from example RGB fundus images : (a) ‘01_test’ from DRIVE, (b) ‘im0077’ from STARE, (c) ‘Image_05L’ from CHASE_DB-1, (d) ‘08_dr’ from HRF dataset.*

work.

For color normalization, we choose a healthy fundus image, in which vessels are in good contrast with the background, as the reference image. Histogram-matching [14] of the input image to the reference image is done, at red, green, and blue channels, individually. An example of color normalization is shown in Figure 2.3. The input fundus image ‘01_test’ (Figure 2.3 (a)) is taken from the test set of the DRIVE dataset. Here, for reference, the fundus image ‘im0077’ (Figure 2.3 (b)) from the healthy set of STARE dataset, is used and Figure 2.3 (c) shows the result after color normalization. It is clear that the resulting image has similar pigmentation as that of the reference image.

Green Channel Extraction

The color normalized fundus image has three channels, out of which red and blue channels are very poorly contrasted and noisy. The corresponding channel pixels do not provide much information regarding blood vessels. Whereas, green channel has the best contrast between vessel pixels and non-vessel background pixels. Thus, for blood vessel extraction, only the green channel of the RGB image is used for further

processing [6].

Now, we have the green channel of color-equalized RoI of fundus image, $I_{green}(x, y)$. This completes the pre-processing stage, and the image is ready for core processing.

2.2.2 Core processing : Gray-scale Vessel Enhancement

This sub-section describes the most important part of our proposed vessel segmentation algorithm. It uniquely handles both thin and thick vessels. Blood vessels are examples of curve singularities. The curves at the global image-level appear almost linear at the local sub-image level. This is the key motivation of our algorithm. After pre-processing, the proposed algorithm works, broadly, in two steps,

- Multiscale vessel-enhancement using directional wavelets (locally) and curvelets (globally),
- Vessel thickness-correction using gray-scale morphology.

The following sub-sections discuss the proposed core-processing in detail.

Preparing the Sub-Images for Local Application of Wavelet Transform

The core algorithm starts with dividing the pre-processed green channel image, $I_{green}(x, y)$ into overlapping sub-images. The image is divided into r rows and c columns, producing N sub-images. Two adjacent sub-images have an overlapping width of p pixels,

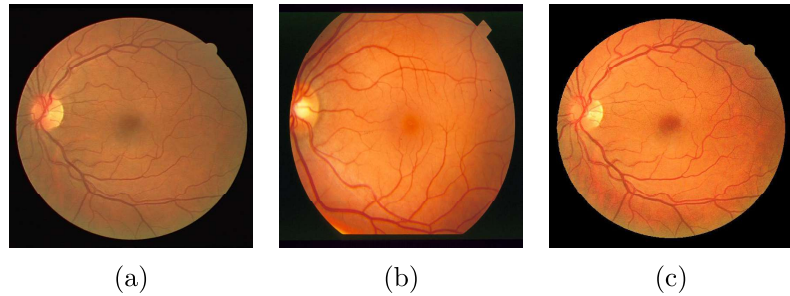


Figure 2.3: *Color normalization* : (a) ‘01_test’ image from DRIVE dataset as input, (b) ‘im0077’ image from STARE dataset as reference, (c) Output fundus after matching input to the reference.

both in the vertical and horizontal direction. Overlapping helps in avoiding blocking effects, thus leading to smooth combined output.

The sub-image at i^{th} row and j^{th} column is denoted by $I_{i,j}(x, y)$, where $1 \leq i \leq r$ and $1 \leq j \leq c$. For further processing, we invert the sub-image to obtain $I'_{i,j}(x, y)$ and apply top-hat transform using a ball-shaped structuring element. This gives us $I^T_{i,j}(x, y)$ with bright vessels in dark background. Figure 2.4 (a) denotes an example sub-image $I_{3,2}(x, y)$ taken from ‘01_test’ of DRIVE dataset, corresponding intensity inverted sub-image $I'_{3,2}(x, y)$ is shown in Figure 2.4 (b). The resulting top-hat transformed sub-image $I^T_{3,2}(x, y)$ is shown in Figure 2.4 (c). After this step, blood vessels become bright and can be more easily extracted as compared to the earlier case shown in Figure 2.4 (a).

Color Normalization

After ROI extraction, another important pre-processing step is to normalize color information of fundus images belonging to different databases. In the real world, images are captured differently. The difference in imaging conditions like camera used, light illumination of the nearby area, geographical location of the experiment, age group of the subject are some factors that make images of each dataset different. Though the basic anatomy of the eye remains the same, color values, dimensions, and intensity illumination may vary. Thus, this step of normalization is important to generalize our work.

For color normalization, we choose a healthy fundus image, in which vessels are in good contrast with the background, as the reference image. Histogram-matching [14] of the input image to the reference image is done, at red, green, and blue channels, individually. An example of color normalization is shown in Figure 2.3. The input fundus image ‘01_test’ (Figure 2.3 (a)) is taken from the test set of the DRIVE dataset. Here, for reference, the fundus image ‘im0077’ (Figure 2.3 (b)) from the healthy set of STARE dataset, is used and Figure 2.3 (c) shows the result after color normalization. It is clear that the resulting image has similar pigmentation as that of the reference image.

Vessel Enhancement using Continuous Wavelet Transform

Now, we have a top-hat transformed sub-image, $I_{i,j}^T(x, y)$. We apply 2-D Continuous Wavelet Transform (CWT) on this sub-image. The standard definitions and notations related to wavelets are given in [23]. Basically, image analysis using wavelets means projecting the subject image on a family of wavelets, where this family is derived from a single mother wavelet by applying translations, dilations, and rotations on it.

Choice of the mother wavelet is a significant step of wavelet analysis. Blood vessels are oriented structures. In the case of such an orientation-specific application, the mother wavelet has to be direction-sensitive. If the mother wavelet is oriented, the wavelet transform obtained has very good directional sensitivity. This helps in detecting directional features with better efficiency. Two such examples of directional wavelets are the 2-D Mexican hat and the 2-D Gabor wavelet. Studies have shown that the Gabor wavelet has better sensitivity for directional features as compared to Mexican hat [23]. Therefore, we have used the 2-D Gabor wavelet as the analyzing (mother) wavelet. Gabor wavelet is a Gaussian modulated complex exponential function. This Gaussian function can be elongated in any one of the directions to make the wavelet anisotropic.

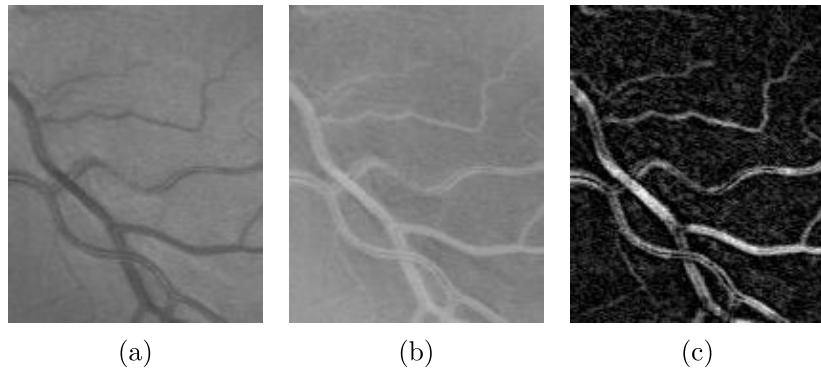


Figure 2.4: *Top-hat transformation on green channel sub-image $I_{3,2}(x, y)$ from ‘01-test’ of DRIVE dataset :* (a) Green channel sub-image, (b) Inverted green channel sub-image, (c) Top-hat transformed sub-image.

Let $\psi(\mathbf{x})$ denotes the 2-D continuous Gabor mother wavelet, given as,

$$\psi(\mathbf{x}) = \exp(j\mathbf{k}_0 \mathbf{x}) \exp\left(-\frac{1}{2}|A\mathbf{x}|^2\right) \quad (2.3)$$

where \mathbf{x} is $(x, y) \in \mathbb{R}^2$, \mathbf{k}_0 is the wave vector defining the frequency of complex exponential, $A = \text{diag}[\epsilon^{-1/2}, 1]$ is a 2×2 positive definite matrix, with $\epsilon \geq 1$ making the function anisotropic [23].

A family of wavelets $\psi_{\mathbf{b}, \theta, a}(x, y)$ can be defined by translations (\mathbf{b}), rotations (θ) and dilations (a) of the mother wavelet $\psi(x, y)$. For each sub-image, the CWT, denoted by, $I_{i,j}^\psi(\mathbf{b}, \theta, a)$ is defined in terms of the scalar product $\langle \cdot, \cdot \rangle$ of $I_{i,j}^T(x, y)$ with the transformed mother wavelet $\psi_{\mathbf{b}, \theta, a}(x, y)$,

$$I_{i,j}^\psi(\mathbf{b}, \theta, a) = C_\psi^{-1/2} \langle \psi_{\mathbf{b}, \theta, a}(x, y), I_{i,j}^T(x, y) \rangle, \forall (x, y) \quad (2.4)$$

where, C_ψ , ψ , \mathbf{b} , θ and a denote the normalizing constant, mother wavelet, displacement vector, rotation angle, and dilation parameter (also known as scale), respectively.

We observe that the magnitude of real coefficients of obtained CWT is more effective in the extraction of thin vessels in comparison to the imaginary or absolute values of these coefficients. Thus, for enhancement of vessel structure, the magnitude of the maximum of real response is calculated for each pixel of the sub-image, over all orientations, θ . Figure 2.5 shows the evaluated wavelet response magnitude at scales $a = 1, 2, 3$ and 4 of an example sub-image ($i=3, j=2$) from image ‘01_test’ of DRIVE dataset. As can be clearly seen from Figure 2.5 (a), at scale $a_1=1$, only a few fine details are enhanced, which includes both vessel and non-vessel pixels equally, and Figure 2.5 (d) shows unwanted merging and blurring of the vessel and non-vessel pixels, at scale $a_4=4$. Whereas, at scales, $a_2=2$ and $a_3=3$, vessel edges are most sharp with suppressed non-vessel edges, shown in Figure 2.5 (b) and (c), respectively. Though shown only for one image, it was observed for almost all the images. Thus, we have considered only two scales $a_2=2$ and $a_3=3$.

The summation of magnitudes of maximum of real responses at these two scales is

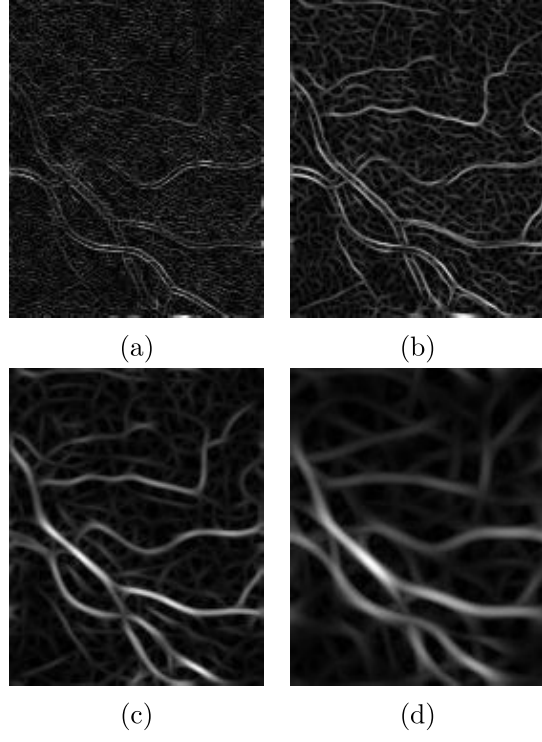


Figure 2.5: *Magnitude of maximum of real response of the sub-image $I_{3,2}(x, y)$ from ‘01_test’ of DRIVE dataset at different scales :* (a) $a_1 = 1$, (b) $a_2 = 2$, (b) $a_3 = 3$, (b) $a_4 = 4$.

given by $M_{i,j}^\psi(\mathbf{b})$ which is,

$$M_{i,j}^\psi(\mathbf{b}) = \left| \max_\theta \left[\operatorname{Re}\{I_{i,j}^\psi(\mathbf{b}, \theta, a_2)\} \right] \right| + \left| \max_\theta \left[\operatorname{Re}\{I_{i,j}^\psi(\mathbf{b}, \theta, a_3)\} \right] \right|, \forall(i, j) \quad (2.5)$$

This magnitude response is re-normalized in the range of $[0, 1]$. Normalized magnitude responses corresponding to all the sub-images are integrated together and contrast-enhanced to re-construct the original-sized magnitude response image, denoted by $I_M^\psi(x, y)$, shown in Figure 2.6 (a). Now, we have a wavelet enhanced, gray-scale vessel map to be processed further.

Contrast Enhancement using Discrete Curvelet Transform

Wavelet transform has enhanced all types of locally linear and oriented structures, including some false, vessel-like edges of background too. To suppress these features of background, we need another step of vessel enhancement. For this purpose, we apply Discrete Curvelet transform (DCuT) [15], [16] on this wavelet enhanced response image globally. DCuT is another multi-scale transform that is used as a high-boost filter in this work.

It converts an image into sub-bands with different scales and orientations using polar, wedge-shaped windows in the frequency domain. These windows make the transform highly anisotropic and direction sensitive, thus very efficiently enhancing omni-directional curved blood vessels.

The wavelet enhanced gray-scale vessel map $I_M^\psi(x, y)$ is decomposed into a superposition of L images as,

$$I_M^\psi(x, y) = D_L(x, y) + \sum_{l=1}^{L-1} D_l(x, y), \forall(x, y) \quad (2.6)$$

where, $D_L(x, y)$ is the coarsest version of input image (Figure 2.6 (b)) and summation of $D_l(x, y)$ over all $l \in [1, L - 1]$ denotes the remaining portion (Figure 2.6 (c)).

For vessel enhancement, the contribution of the coarsest scale ($l=L$) is made zero i.e. we put $D_L(x, y)=0$ and the remaining fine scale contributions ($1 \leq l \leq L - 1$) are kept the same to obtain $I_C(x, y)$ which gives us the curved edges,

$$I_C(x, y) = \sum_{l=1}^{L-1} D_l(x, y), \forall(x, y) \quad (2.7)$$

The obtained gray-scale image corresponding to the curved details $I_C(x, y)$ (shown in Figure 2.6 (c)) is superimposed on the gray-scale wavelet response image $I_M^\psi(x, y)$ (Figure 2.6 (a)) to obtain vessel enhanced gray-scale image $I_{VE}(x, y)$ (Figure 2.6 (d)),

$$I_{VE}(x, y) = I_M^\psi(x, y) + I_C(x, y), \forall(x, y) \quad (2.8)$$

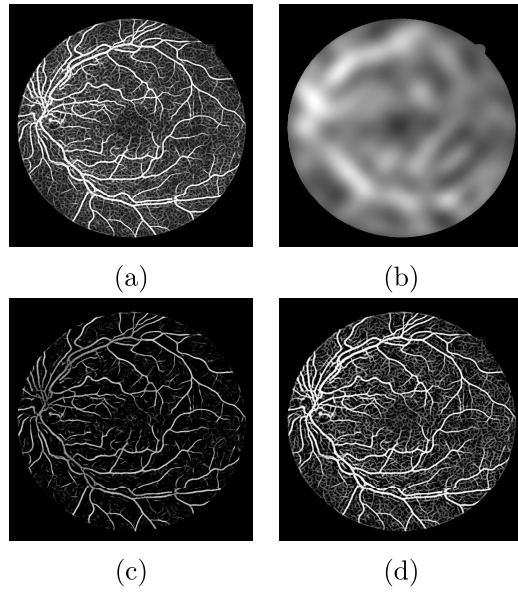


Figure 2.6: *Illustration of contrast enhancement using DCuT* : (a) Combined wavelet response image, $I_M^\psi(x, y)$, (b) Coarsest version of wavelet response image, $D_L(x, y)$, (c) Remaining image containing the details, $I_C(x, y)$, (d) Resulting contrast-enhanced image, $I_{VE}(x, y)$.

This step is a kind of high boost filtering in which edges are extracted using DCuT and again added to the wavelet enhanced gray-scale vessel map to obtain a sharper vessel map.

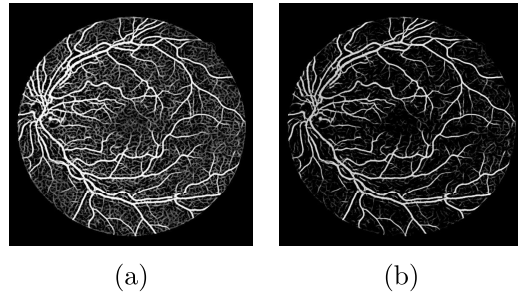


Figure 2.7: *Background texture removal* : (a) Contrast enhanced vessel map obtained using DCuT, $I_{VE}(x, y)$, (b) Thin vessel map obtained after removing non-vessel background texture, $I_{thin}(x, y)$.

Background Texture Removal

After DCuT based gray-scale contrast enhancement, next is a background texture removal step using Gaussian blurring. This is an isotropic step. To remove the fine noisy texture of background, we take a difference between $I_{VE}(x, y)$ and its blurred version, obtained using a large size ($K \times K$) averaging kernel [32]. For this purpose, we use a zero mean Gaussian kernel as a mean filter to average the pixel intensity values. The difference gives an enhanced thin-vessel map denoted by $I_{thin}(x, y)$ and is given as,

$$I_{thin}(x, y) = I_{VE}(x, y) - I_{blur}(x, y), \forall(x, y) \quad (2.9)$$

where, $I_{blur}(x, y)$ denotes the image background produced by large kernel Gaussian blurring.

At this stage, we have obtained $I_{thin}(x, y)$, which is a gray-scale fundus image with retinal vessels up to a very fine level, shown in Figure 2.7 (b). This image is almost free from fine background texture. Till this stage, our complete focus has been on fine vessel extraction. We may have lost some boundary pixels of thick vessels. In the next step, we apply a thickness-correction, morphological step on our original inverted green channel fundus image to recover the thickness of major vessels.

Vessel Thickness-Correction using Gray-scale Morphology

Multiscaling has allowed us to enhance the fine vessel map. To improve the accuracy of this segmentation algorithm, we apply a global morphological step to extract the major vessel arcade. In section 2.2.2, a similar initial operation was performed, but, there the focus was on the extraction of thin and fragile vessels. Previously, it was applied at the sub-image level using a smaller structuring element. Here, we implement a similar operation but with a bigger structuring element to extract thick vessels. The size of the structuring element is decided with the help of a binary FoV mask derived during pre-processing. The large diameter of FoV implies the need for a bigger structuring element to cover the thickest vessels. The pre-processed green channel is first inverted $I'_{green}(x, y)$, contrast is enhanced using CLAHE [44], and then top-hat

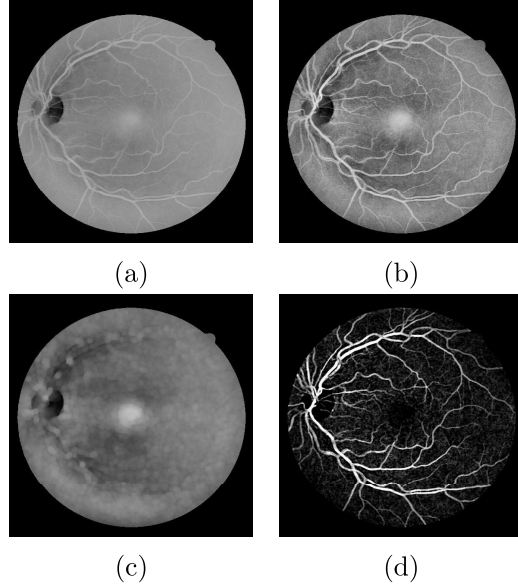


Figure 2.8: *Gray-scale Morphological extraction of major vessel arcade* : (a) Inverted green channel image, (b) Contrast enhanced image, (c) Image after Morphological opening, (d) Top-hat transformation of contrast enhanced image.

transformation [14] is applied using a ball-shaped structuring element. The resulting gray-scale output has enhanced the thick vessel map, and it is termed as $I_{thick}(x, y)$. These morphological steps are shown in Figure 2.8.

Now, we have two gray-scale vessel maps corresponding to thin and thick vessels, $I_{thin}(x, y)$ and $I_{thick}(x, y)$ shown in Figure 2.9 (a) and (b), respectively. Figure 2.9 (c) shows the result after pixel-wise addition and re-normalization of these two vessel maps given by $I_{vessel}(x, y)$,

$$I_{vessel}(x, y) = I_{thin}(x, y) + I_{thick}(x, y), \forall(x, y) \quad (2.10)$$

Thus, we have extracted a gray-scale vessel map with recovered vessel widths. It has a complete vessel map, including both thin and thick vessels. Next is the post-processing step to produce the final refined binary vessel map.

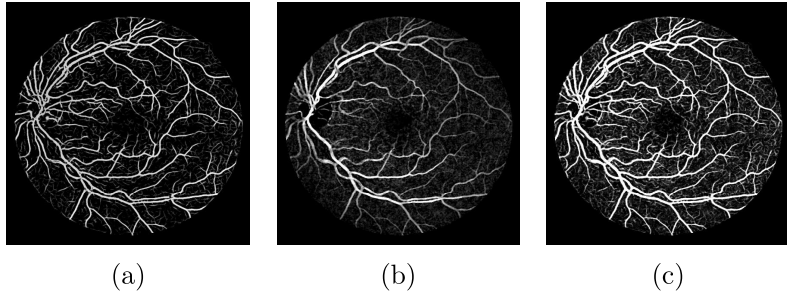


Figure 2.9: *Vessel-width correction* : (a) $I_{thin}(x, y)$, (b) $I_{thick}(x, y)$, (c) $I_{vessel}(x, y)$.

2.2.3 Post-processing

Post-processing refines the output vessel map to its final form. It consists of three simple steps,

- Thresholding of gray-scale vessel map using Otsu’s method [47], Figure 2.10 (a),
- Removing small isolated components using morphological area opening, Figure 2.10 (b),
- Removing small parasitic branches using morphological image pruning, Figure 2.10 (c).

To summarize, in this work, the only input is the RGB fundus image which is pre-processed in three steps: ROI extraction, color-normalization, and green channel extraction. Then, two multi-scale transforms, wavelets (on sub-images) and curvelets (on complete image), are applied sequentially on the pre-processed image. To recover the actual vessel widths, a morphologically segmented vessel map is added to the enhanced vessel map. Thresholding, area opening, and pruning are three post-processing steps used in the end.

2.3 Materials and Metrics

The proposed algorithm is tested on four different fundus image datasets available in the public domain. These are : DRIVE [11], STARE [8], CHASE_DB-1 [13] and HRF [48]. Each set has a different number of images, dimensions, FoV, illumination,

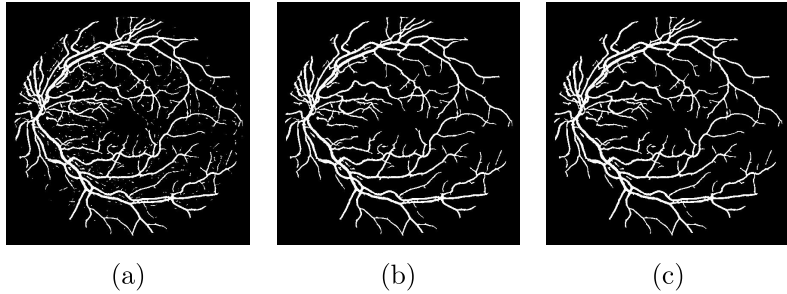


Figure 2.10: *Post-processing steps* : (a) Output binary vessel map, (b) Vessel map after morphological area opening, (c) Vessel map after morphological pruning.

and pigmentation. Testing on such a variety of data has helped in developing a robust and generic algorithm. In DRIVE, STARE, and CHASE_DB-1 datasets, annotations are done by two experts (Expert-1 and Expert-2), whereas in the HRF dataset, only one expert annotation is provided. But, almost all the researchers in this field use annotations done by Expert-1 for performance evaluation. Thus, to present a fair comparison with others, we have also used the same annotations.

The presented vessel segmentation algorithm is an unsupervised classification of each pixel of the fundus image into two classes: vessel pixel or non-vessel pixel. These classes are highly imbalanced because background (non-vessel) pixels are very high in number compared to vessel pixels. Even after the ROI extraction and thereby removing many non-informative, non-vessel pixels, this imbalance still prevails. Inside the FoV of a fundus image, only about 13% of the total pixels are vessel pixels, and the rest are non-vessels. This significant imbalance in data makes the choice of a valid performance measure very important. Thus, for a fair evaluation and comparison of our work with other existing works, the proposed algorithm is evaluated in terms of eight measures, Accuracy (Acc), Sensitivity (Sen), Specificity (Spe), Precision (Pr), F-1 score ($F1$), G-mean (G), Matthews Correlation Coefficient (MCC) and Area Under (AUC) the Receiver Operating Characteristic curve (ROC). These metrics are defined in terms of True Positives (TP), True Negatives (TN), False Positives (FP) and False Negatives (FN), described as,

- **TP** : Number of image pixels correctly identified as vessel pixels.

- **TN** : Number of image pixels correctly identified as non-vessel pixels.
- **FP** : Number of image pixels wrongly identified as vessel pixels.
- **FN** : Number of image pixels wrongly identified as non-vessel pixels.

$$Acc = \frac{(TP + TN)}{(TP + TN + FP + FN)} \quad (2.11)$$

$$Sen = \frac{(TP)}{(TP + FN)} = TPR \quad (2.12)$$

$$Spe = \frac{(TN)}{(TN + FP)} = 1 - FPR \quad (2.13)$$

$$Pr = \frac{(TP)}{(TP + FP)} \quad (2.14)$$

$$F1 = \frac{(2 \times Pr \times Sen)}{(Pr + Sen)} \quad (2.15)$$

$$G = \sqrt{Sen \times Spe} \quad (2.16)$$

$$MCC = \frac{TP/N - S \times P}{\sqrt{P \times S \times (1 - S) \times (1 - P)}} \quad (2.17)$$

Here, TPR : True Positive Rate, FPR : False Positive Rate, $N = TP + TN + FP + FN$: total number of pixels inside FoV, $S = (TP + FN)/N$ and $P = (TP + FP)/N$.

The presented work deals with the semantic segmentation of medical images. The medical data, in itself, is subjective, and along with that, we need to consider the major pixel imbalance while segmenting the vessels. As already mentioned, the choice of an appropriate performance metrics is crucial in this case. For instance, if we compare two vessel segmentation algorithms, the first algorithm segments only the thick vessels and misses out all the thin vessels. In contrast, the second one segments a complete vessel map including all the thick and thin vessels, both the algorithms will have an

almost similar value of TP . This is because the contribution of thin vessels in the value of TP is negligible or significantly less. Also, fundus images have a majority of background (non-vessel) pixels. Thus there is always a chance of getting a high value of TN . Thus, values of Acc and Spe can be slightly misleading for the evaluation of our algorithm. Also, to minimize the risk of the wrong diagnosis, we try to keep FN as low as possible. This makes Sen an important measure. Other measures, which do not depend directly on TN , can also correctly evaluate such an imbalanced data classification algorithm. G -mean combines Sen and Spe metrics in the form of the geometric mean. Pr is another measure. It tells about the correctness of the classified vessel pixels, i.e., how many TP are there in the total number of positives. $F1$ -score incorporates both Pr and Sen as harmonic mean. MCC is another metric used. It is a correlation coefficient between the predicted classes and manual classification. AUC under the ROC curve is a statistical performance metric. ROC is a plot between Sen (or TPR) and $1 - Spe$ (or FPR) of a classification algorithm, obtained by varying one of its parameters. In our work, this parameter is the intensity threshold. ROC curve shows a trade-off between the above two metrics. AUC helps in evaluating the classification ability of an algorithm. A higher value of AUC means the ROC reaches the coordinate $(0,1)$, which leads to 0% FPR and 100% TPR , characteristics of an ideal classifier.

2.4 Experiments and Discussions

This section discusses the results of the proposed algorithm and its comparative performance with respect to other existing methods. For a better visual comparison, the segmented vessel map, marked in green color, is superimposed on the manual annotations, marked in red color.

2.4.1 Results

The algorithm is tested on all the labeled images available in the above-mentioned databases. Figure 2.11 shows the comparative segmentation results on a healthy fundus

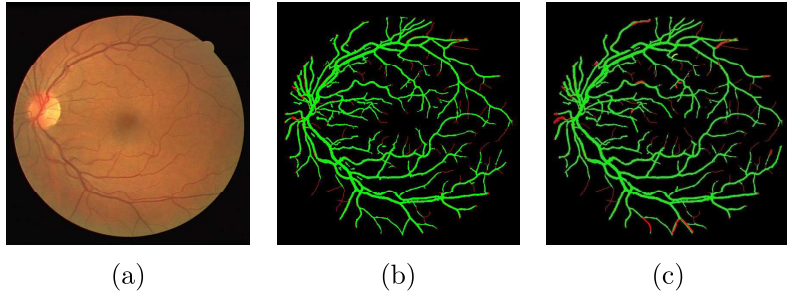


Figure 2.11: Comparison of the output vessel segmentation on image ‘01_test’ from DRIVE dataset using the proposed method and the nearest best performing method Orlando et al. [41]. The obtained vessel map is shown in green w.r.t. the ground truth in red. The color coding facilitates in viewing the missed vessels. The proposed method has been successful in extracting the complete vessel map except some very fine vessel ends, visible in red. The other method is observed to be missing out on fine vessels. (a) Result of proposed method, (b) Result of nearest best method.

image, ‘01_test’, taken from the DRIVE dataset. Table 2.1 presents the obtained values of all performance metrics w.r.t expert-1 and 2, for image ‘01_test’ of DRIVE dataset.

Figure 2.12 shows the comparison of mean ROC curves of the proposed method on four datasets. The performance of Expert-2 (in the case of DRIVE, STARE, and CHASE_DB-1) is plotted using solid marker points in the same figure. The closeness of these four ROC curves proves the statistical consistency of the proposed algorithm on different datasets. Maximum *AUC* is achieved on STARE dataset with a value of 0.966 and minimum on CHASE_DB-1 with value 0.953. CHASE_DB-1 is a high-resolution database having images almost 2.26 times bigger than images of the STARE dataset. This small difference value of 0.013 supports the point of the robustness of the proposed algorithm.

Figure 2.13 and Figure 2.14 show comparative vessel segmentation results corresponding to a few sample pathological fundus images. Figure 2.13 (a,b,c) is an ex-

Table 2.1: Performance of proposed algorithm on image ‘01_test’ from DRIVE dataset (a healthy fundus)

Expert	Acc	Sen	Spe	Pr	F1	G	MCC	AUC
Expert-1	0.9612	0.8666	0.9705	0.7419	0.7994	0.9171	0.7810	0.9751
Expert-2	0.9615	0.8758	0.9697	0.7346	0.7990	0.9215	0.7816	0.9771

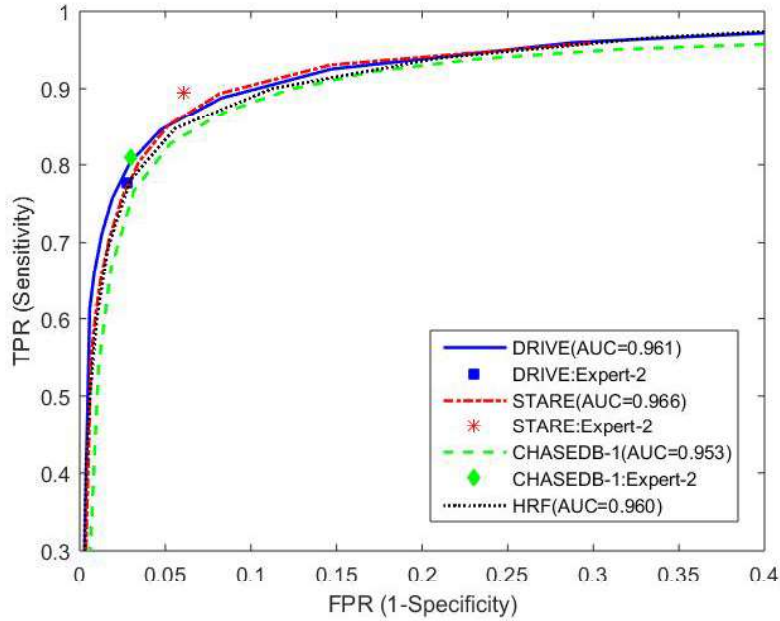


Figure 2.12: *Comparison of mean ROC curves of proposed algorithm on different datasets.*

ample image from DRIVE dataset, with presence of red lesions. It illustrates image ‘14_test’, and its corresponding segmented vessel maps from the proposed method and the nearest best method [41]. We observe a better vessel map extraction (upto fine vessels), even in the presence of abnormality. Similarly, Figure 2.13 (d,e,f) shows image ‘im0044’ from the STARE dataset, and the corresponding results. Here, we observe a bright flashy patch, which disturbs the contrast of vessels. The proposed algorithm has managed to extract a continuous vessel map, including the fine vessels whereas the other nearest best method [33] loses some parts of major vessels and fine vessels. Figure 2.14 (a,b,c) correspond to ‘Image_05L’ from CHASE_DB-1 dataset, the proposed segmented vessel map, and the nearest method vessel map [45], respectively. Figure 2.14 (d,e,f) shows HRF image ‘07_dr’, proposed segmented vessel map, and the nearest method vessel map [50], respectively. Here also, the fine vessels are better segmented in comparison to other methods. As clearly seen, these images are some challenging samples taken from the datasets, and the proposed algorithm has performed well on all the four cases. In terms of sensitivity metric, the values obtained are 0.970, 0.973,

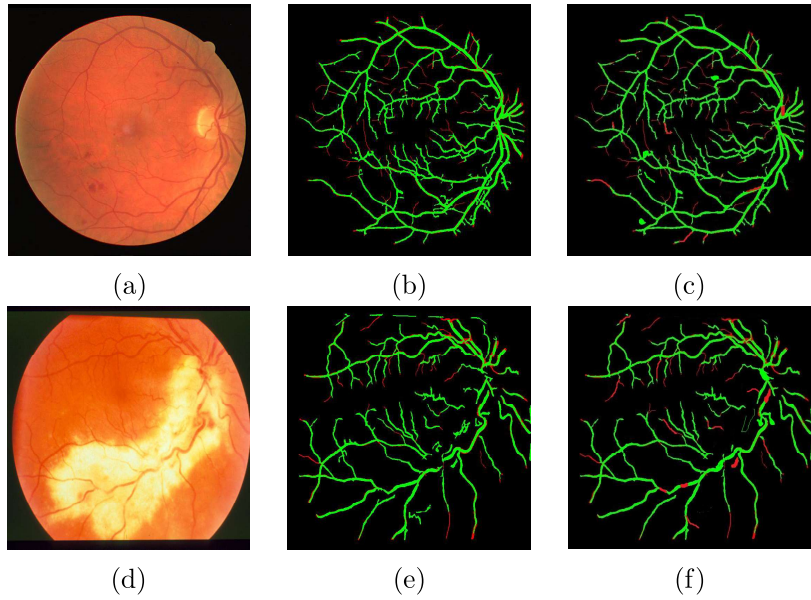


Figure 2.13: *Comparative vessel segmentation results on sample pathological images, ‘14_test’ from DRIVE and ‘im0044’ from STARE datasets. The proposed method shows a promising vessel extraction even in the presence of red lesions on DRIVE data image, as it has not misidentified the red lesions as vessels, as done by the nearest best method [41]. The sample STARE image has challenging bright region where the proposed method has been successful in extracting a better continuous vessel map and fine vessels as compared to the nearest best method [33]: (a,b,c) Comparison on DRIVE image, (d,e,f) Comparison on STARE image.*

0.818, and 0.973, respectively, which depict an outstanding vessel map extraction in such challenging images. Performance measures corresponding to all these images are given in Table 2.2 (w.r.t. the annotations of Expert-1 in case of DRIVE, STARE, and CHASE_DB-1 datasets).

Table 2.2: Performance of proposed algorithm on some pathological images of publicly available datasets w.r.t. Expert-1 (in case, more than one expert annotations available)

Image Label	Dataset	Acc	Sen	Spe	Pr	F1	G	MCC	AUC
14_test	DRIVE	0.958	0.970	0.828	0.706	0.762	0.896	0.742	0.963
im0044	STARE	0.962	0.973	0.813	0.697	0.751	0.890	0.733	0.972
Image_05L	CHASE_DB-1	0.957	0.818	0.969	0.694	0.751	0.890	0.730	0.954
7_dr	HRF	0.962	0.973	0.813	0.697	0.751	0.890	0.733	0.961

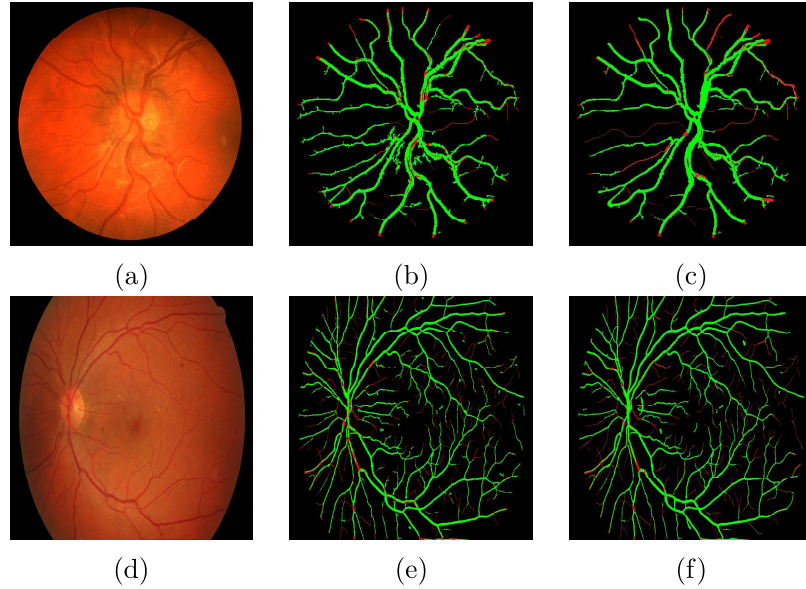


Figure 2.14: *Comparative vessel segmentation results on sample pathological images, ‘Image_05L’ from CHASE_DB-1 and ‘07_dr’ HRF datasets. The proposed algorithm has been successful in extracting vessel maps, including the thin vessels, even in challenging fundus background. The image from CHASE_DB-1 has in-homogeneous illumination, the proposed method has successfully extracted some very fine poor-contrast vessels, whereas the other method [45] could not perform well in such regions. In HRF image, many fine vessels are missed by the nearest best method [50] in comparison to the proposed method: (a,b,c) Comparison on CHASE_DB-1 image, (d,e,f) Comparison on HRF image.*

2.4.2 Discussions

In this section, we have discussed the obtained results and compared the performance of the proposed method with other breakthrough and state-of-the-art vessel extraction methods. Table 2.3 gives this comparison on DRIVE and STARE datasets, and Table 2.4 presents the same on CHASE_DB-1 and HRF datasets. Performance measures corresponding to the vessel map annotated by Expert-2 are given in these tables to standardize the comparison. For a better understanding, Table 2.3 is divided into two sections, supervised and unsupervised methods. The best state-of-the-art value and our result corresponding to each performance measure are highlighted in both tables. These tables depict that the results obtained using the proposed algorithm are either better or very close to the best value of a single column (measure) while maintaining decent values in other columns (measures). This means that our proposed method has been successful in performing well in terms of all eight measures for four different databases. This proves the consistency and robustness of our algorithm.

In the case of the DRIVE dataset, the proposed algorithm has outperformed in terms of G -mean and has performed similarly to the best in terms of Acc and Sen for both supervised and unsupervised algorithms. AUC for ROC is also quite comparable with that of the other methods. STARE dataset has many challenging images (pathological and poor-contrast). The proposed algorithm has performed outstandingly well in terms of Acc and Pr . Also, other measures, $F1$ score and AUC , are comparable with the other state-of-the-art methods. The majority of researchers have presented their work on these two low-resolution datasets only.

Few researchers have given their vessel segmentation results on CHASE_DB-1 and HRF datasets. Thus, a separate comparison table is made for them. These sets have high-resolution images. In the proposed method, we have worked on original-sized images without any down-sampling to avoid any compression losses. This algorithm has performed very well on these high-resolution datasets, too, as compared to other works, as shown in Table 2.4. For CHASE_DB-1, the proposed algorithm has performed better than others in terms of Acc , $F1$ -score, G -mean, and MCC .

Moreover, to evaluate the statistical significance of the proposed algorithm, we

perform the Mann-Whitney test [19]. It is a non-parametric test, where we assume the significance level $\alpha = 0.05$. The obtained p-values are 0.0036, 0.0109, 0.0200, and 0.0017 for DRIVE, STARE, CHASE_DB-1, and HRF datasets, respectively. The p-values less than α prove the reliability of the proposed vessel segmentation method.

Compared to other unsupervised methods, our algorithm has performed better while extracting the complete vessel map, including thin and thick vessels. For instance, Odstrcilik et al. [48] used five different kernels (with different vessel profiles), assuming five possible vessel widths. The choice of such kernels is highly data-dependent. Also, defining a fixed vessel profile for a particular width has made the algorithm very specific. The proposed multi-scale method is simpler and less data-dependent as it uses only two scales to cover the complete vessel map. For thin vessels, an optimized combination of scales is taken while applying wavelets. To recover the lost boundary pixels of thick vessels, morphology has been used. Thus, the thickness of vessels is maintained. Quantitatively, our method has performed better than [48], in terms of *Acc*, *Spe*, *Pr*, *F1* score and *MCC*.

The proposed algorithm is based on conventional, rule-based image processing techniques, which does not depend on any labeled data. It is always ready to go with any new kind of data, making this method very less complex than other supervised methods. For instance, Orlando et al. [41] gave a supervised vessel segmentation algorithm. Such algorithms need re-training with each new dataset which makes them computationally expensive. In [41], the author has also reported some misclassification issues

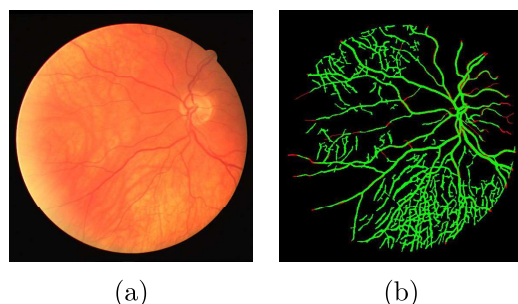


Figure 2.15: *Illustration of failure of proposed algorithm in case of dominant choroidal vessels* : (a) Example fundus image ‘23_training’ of DRIVE dataset, (b) Segmented vessel map in green w.r.t. the ground truth.

Table 2.3: Performance comparison of proposed algorithm on DRIVE and STARE datasets

DATASET Category	Method	DRIVE						STARE									
		Acc	Sen	Spe	Pr	F1	G	MCC	AUC	Acc	Sen	Spe	Pr	F1	G	MCC	AUC
Supervised methods	Expert-2	0.947	0.776	0.973	0.807	0.788	0.868	0.760	-	0.935	0.895	0.939	0.642	0.740	0.917	0.722	-
	Niemeijer et al. [11]	0.942	0.690	0.970	NA	NA	0.818	NA	0.930	NA	NA	NA	NA	NA	NA	NA	NA
	Soares et al. [23]	0.947	0.728	0.979	NA	NA	0.844	NA	0.961	0.948	0.720	0.975	NA	NA	0.838	NA	0.967
	Ricci et al. [24]	0.959	NA	NA	NA	NA	NA	NA	0.963	0.965	NA	NA	NA	NA	NA	NA	0.968
	Marin et al. [32]	0.945	0.707	0.980	NA	NA	0.832	NA	0.958	0.952	0.694	0.982	NA	NA	0.825	NA	0.977
	Liskowski et al. [33]	0.949	0.776	0.977	NA	NA	0.871	NA	0.972	0.957	0.787	0.975	NA	NA	0.876	NA	0.978
	Orlando et al. [41]	NA	0.790	0.968	0.785	0.780	0.874	0.756	0.951	NA	0.768	0.974	0.774	0.764	0.865	0.742	0.971
Unsupervised methods	Yao et al. [50]	0.954	0.765	0.982	NA	NA	0.867	NA	0.975	0.961	0.758	0.985	NA	NA	0.864	NA	0.980
	Staal et al. [10]	0.944	0.719	0.977	NA	NA	0.838	NA	0.952	0.952	0.697	0.977	NA	NA	0.825	NA	0.961
	Mendonca et al. [22]	0.945	0.734	0.976	NA	NA	0.846	NA	0.944	0.699	0.973	NA	NA	0.825	NA	NA	NA
	Zheng et al. [9]	0.938	0.712	0.972	NA	NA	0.832	NA	NA	0.947	0.735	0.973	NA	NA	0.846	NA	NA
	Al Diri et al. [30]	NA	0.728	0.955	NA	NA	0.834	NA	NA	NA	0.752	0.968	NA	NA	0.853	NA	NA
	Miri et al. [28]	0.946	0.735	0.979	NA	NA	0.848	NA	NA	NA	NA	NA	NA	NA	NA	NA	NA
	Fraz et al. [49]	0.942	0.730	0.974	0.811	0.769	0.843	0.736	NA	0.942	0.732	0.966	0.729	0.731	0.841	0.691	NA
	Chakraborti et al. [59]	0.937	0.720	0.958	NA	NA	0.831	NA	0.942	0.938	0.679	0.959	NA	NA	0.806	NA	NA
CHASE_DB-1	Roychowdhury et al. [45]	0.947	0.761	0.957	NA	NA	NA	NA	0.951	0.772	0.973	NA	NA	0.867	NA	0.962	
	Azzopardi et al. [60]	0.939	0.758	0.959	NA	NA	0.844	NA	0.962	0.951	0.772	0.973	NA	NA	0.853	0.680	0.949
	Orlando et al. [41]	NA	0.728	0.971	0.744	0.733	0.841	0.705	0.961	0.950	0.772	0.970	NA	NA	0.865	0.733	0.956
	Proposed method	0.958	0.754	0.975	0.719	0.736	0.858	0.714	0.953								
HRF	Odstrcilik et al. [48]	0.949	0.779	0.965	0.695	0.732	0.867	0.706	0.968								
	Orlando et al. [41]	NA	0.787	0.958	0.663	0.716	0.869	0.690									
	Yan et al. [50]	0.943	0.788	0.959	0.665	NA	0.869	NA									
	Proposed method	0.952	0.750	0.972	0.727	0.733	0.854	0.710	0.960								

Table 2.4: Performance comparison of proposed algorithm on CHASE_DB-1 and HRF datasets

DATASET	Method	Acc	Sen	Spe	Pr	F1	G	MCC	AUC
	Expert-2	0.954	0.742	0.979	0.809	0.769	0.853	0.747	-
CHASE_DB-1	Fraz et al. [9]	0.947	0.722	0.971	0.741	NA	0.837	NA	0.971
	Roychowdhury et al. [45]	0.947	0.761	0.957	NA	NA	0.853	NA	0.962
	Azzopardi et al. [60]	0.939	0.758	0.959	NA	NA	0.853	0.680	0.949
	Orlando et al. [41]	NA	0.728	0.971	0.744	0.733	0.841	0.705	0.948
	Proposed method	0.958	0.754	0.975	0.719	0.736	0.858	0.714	0.953
HRF	Odstrcilik et al. [48]	0.949	0.779	0.965	0.695	0.732	0.867	0.706	0.968
	Orlando et al. [41]	NA	0.787	0.958	0.663	0.716	0.869	0.690	0.952
	Yan et al. [50]	0.943	0.788	0.959	0.665	NA	0.869	NA	NA
	Proposed method	0.952	0.750	0.972	0.727	0.733	0.854	0.710	0.960

while dealing with high-resolution databases like CHASE_DB-1 and HRF. Quantitatively, our method has performed better than [41], in terms of *Spe*, *Pr*, *F1* score and *AUC*. Methods using deep learning require a huge amount of annotated data, which is a big issue in medical images. With a Xeon W-2195, 2.30GHz processor, the mean computational time for the proposed pipeline was 0.47 s, 0.64 s, 0.77 s, and 0.81 s for DRIVE, STARE, CHASE_DB-1, and HRF datasets, respectively.

In the presented algorithm, the resulting images show the segmentation of almost every kind of vessel: thick, thin and fine, even in poor-contrast, pathological environment. Multi-scaling has allowed us to reach the fine vessels with better precision in a poorly contrasted background. The use of real coefficients of the directional wavelet transform at the sub-image level has helped us extract fine vessels with sharpness, even in low-contrast regions. DCuT at the global level has helped fine-tune the obtained

wavelet enhanced vessel image by contrast-enhancement. The morphological extraction of prominent vessels leads to the recovery of the thickness of prominent vessels.

The main parameters of the proposed algorithm are choice of mother wavelet, scale values (a) in wavelet analysis, level values (L) in curvelet analysis, and the size of ‘ball-shaped’ structuring element in the morphological thickness correction step. Fine-tuning of these parameters is necessary to obtain the best vessel map. As the vessels are directional features of retinal images, choosing a directional analyzing wavelet is inevitable. We use a 2-D Gabor wavelet for this purpose in our work. For high-resolution fundus images, a higher value of scale parameter is needed to cover the thicker vessels. Likewise, the maximum level value and size of the structuring element increases with an increase in resolution of the input fundus image. The diameter of the derived FoV mask estimates the fundus resolution, and hence the parameter values are decided.

Some subjects have a thin retinal layer. In such cases, choroidal vessels are quite visible in fundus images. Figure 2.15 depicts one such case in which the proposed algorithm fails. This figure shows the image ‘23_training’ taken from the DRIVE dataset. It has prominently visible background choroidal vessels, which look almost similar to the retinal blood vessels. Generally, these vessels are hidden but sometimes become prominently visible in some of the subjects. Researchers have not presented their results on such images to the best of our knowledge. Till now, the proposed method is not able to distinguish between these two kinds of the vasculature. We are trying to get a better understanding of such vessels to improve our algorithm.

2.5 Chapter Summary

This chapter presents an unsupervised, multi-scale vessel extraction technique using conventional image processing methods. This work focuses on the segmentation of fine vessel ends while segmenting the retinal vessel map. The implications of losing the vessel ends involves rise in false positives while segmenting the DR-specific red lesions (further discussed in chapter 4), and misinterpretation of neovascularization,

which is a severe stage of DR in which the vessels become fragile and start dividing into multiple vessels (future work). Moreover, we add a thickness-correction step to recover the boundary vessel pixels and thus, recovering the vessel width. As the data is already skewed, to focus on the fine vessels and boundary pixels, we maximize the sensitivity parameter while maintaining the other performance metrics comparable to the state-of-the-art values.

The presented algorithm has been experimented with a wide variety of data, with different ranges of resolution, color, and FoV's. With the target of generalizing an unsupervised algorithm over such a variety, we have been successful in achieving an average sensitivity of 0.764 and AUC of 0.960, while maintaining the average accuracy as 0.957, which is comparable to the state-of-the-art methods. Performance-wise, the proposed method has outperformed even many supervised state-of-the-art methods. This method can efficiently extract the complete vessel map, including both thick and thin vessels, without any data labeling. The immediate next chapter will introduce deep learning to improve vessel extraction in various challenging fundus backgrounds.